Journal of Materials Research and Technology 43 (2026) 2788–2800

Contents lists available at ScienceDirect

Journal of Materials Research and Technology

journal homepage: www.elsevier.com/locate/jmrt

Understanding the processing pathway on the vitrification behavior of Zr-based bulk metallic glasses: The case of Vit106a

Damien Terebenec [a,*], Markus Mohr [b,c], Robert Zboray [a,d], Stephan Schneider [b], Alex Dommann [a,d], Antonia Neels [a,e,**]

[a] Center for X-ray Analytics, Empa, Swiss Federal Laboratories for Materials Science and Technology, Dübendorf, Switzerland
[b] Institute of Quantum Technologies, German Aerospace Center (DLR), Ulm, Germany
[c] Institute of Functional Nanosystems, University of Ulm, Ulm, Germany
[d] ARTORG Center for Biomedical Engineering Research, University of Bern, Bern, Switzerland
[e] Department of Chemistry, University of Fribourg, Fribourg, Switzerland

ARTICLE INFO

Keywords:
Bulk metallic glass
Microgravity
Electromagnetic levitation
Vitrification

ABSTRACT

In this study, we investigate the effects of thermal history, gravitational environment, and processing conditions on the vitrification and crystallization behavior of Vit106a bulk metallic glass (BMG) alloys. Samples were processed either on ground using arc melting, or in short-term and long-term microgravity conditions in parabolic flight and aboard the International Space Station (ISS) using electromagnetic levitation (EML). Despite employing a two-step synthesis approach with a Nb–Ni pre-alloy, large Nb-rich regions were observed in the lower sections of Earth and parabolic flight samples, indicating gravitational segregation of Nb due to its high density and limited reactivity. In contrast, no such segregation was observed in the ISS-processed sample, suggesting that microgravity, possibly suppressed density-driven separation. The critical cooling rate for achieving vitrification in a 6.5 mm diameter Vit106a sphere exceeds 30 K s^{-1}, much higher than previously reported for smaller samples of 2 mm diameter, highlighting the scale sensitivity of vitrification probably due to strong sensitivity to heterogenous nucleation. However, glass-forming ability cannot be described only by cooling rate. Our results demonstrate that liquid-state processing conditions play a decisive role in governing subsequent crystallization behavior. In particular, sinusoidal thermal modulation combined with high overheating temperatures (above ~1275 K) markedly extends the supercooled liquid region, with reductions in crystallization temperature of up to 80 K. Our findings underscore the combined influence of microgravity, overheating temperature, and thermal modulation in controlling liquid-phase behavior and optimizing processing conditions for bulk metallic glass formation at large scales.

1. Introduction

Unlike conventional metals, Bulk metallic glasses (BMGs) lack a long-range ordered atomic structure, which contribute to their unique combination of properties, including exceptionally high strength, large elastic strain limits, and superior corrosion and wear resistance. The glass-forming ability (GFA) of a metallic alloy is mainly defined by its critical cooling rate and is strongly influenced by its atomic composition [1]. According to Inoue's empirical rules, high GFA is favored in multi-component systems (>3 components) with significant atomic size mismatches ($\Delta Z \geq 12\%$) and negative heat of mixing ($\Delta H_{mix} < 0$), as these factors disrupt crystallization and promote glass formation [1]. Additionally, processing the material requires a larger undercooling temperature range, $\Delta T = T_x$-T_g, where T_x is the crystallization temperature and T_g the glass transition temperature. Therefore, identifying metallic alloy compositions with enhanced GFA and a broader processing window is essential for advancing manufacturing capabilities. However, as the casting thickness increases, the metallic melt becomes more susceptible to crystallization during undercooling, making it more challenging to fabricate industrial BMG components with larger casting diameters [2].

Zr-based BMGs have been extensively studied and have

* Corresponding author.
** Corresponding author. Center for X-ray analytics, Empa, Swiss Federal Laboratories for Materials Science and Technology, Dübendorf, Switzerland.
E-mail addresses: Damien.terebenec@empa.ch (D. Terebenec), Antonia.Neels@empa.ch (A. Neels).

https://doi.org/10.1016/j.jmrt.2026.06.151
Received 15 April 2026; Received in revised form 27 May 2026; Accepted 16 June 2026
Available online 18 June 2026

demonstrated excellent potential for forming fully amorphous structures at relatively large casting thickness. The first Zr-based BMG, known as Vitreloy 1 (Vit1), with the composition $Zr_{41}Ti_{14}Cu_{12.5}Ni_{10}Be_{22.5}$, exhibited a critical cooling rate of approximately 1–2 K s^{-1} for a sphere of 2 mm in diameter [3,4]. Since its discovery, numerous new Vitreloy alloys have been developed. One notable advancement is Vit106a ($Zr_{58.5}Cu_{15.6}Ni_{12.8}Al_{10.3}Nb_{2.8}$), a refined version of the earlier Vit106 alloy. This composition incorporates slight adjustments in the Zr–Nb and Cu–Ni–Al ratios, resulting in significantly enhanced GFA and thermal stability [5]. Vit106a exhibits a wide supercooled liquid region (ΔT = 102 K) and can be vitrified with a critical cooling rate as low as 1.75 K s^{-1}, allowing for the fabrication of castings sphere of 2 mm in diameter (30 – 45 mg) [5]. These characteristics make Vit106a one of the best beryllium-free Zr-based BMGs currently available.

The Vitreloy alloy family exhibits several noteworthy characteristics, particularly in their liquid-state behavior. One prominent feature is their strong-to-fragile transition, which has been attributed to a liquid–liquid phase transition involving a structural shift from a low-density to a high-density liquid state [6–8]. This transition significantly alters the temperature dependence of viscosity and is reflected in a shift of the fragility index D^*. Specifically, Zr-based BMG formers demonstrate a change in D^* from approximately 10 (fragile-liquid) at high temperatures to values around 20–30 (strong-liquid) near the glass transition temperature T_g [9–13]. In the case of Vit1, a pronounced shear-thinning effect has also been observed in the liquid state. The shear-thinning behavior has been attributed to the disruption of short- and medium-range atomic order in the liquid, caused by both shear deformation and elevated temperature, which promotes the liquid-liquid structural transition [14]. In contrast, other Vitreloy alloys such as Vit101, Vit105, Vit106, and Vit106a do not exhibit shear-thinning under comparable conditions. It has been suggested that these alloys may already reside in a fragile-liquid state in the temperature range studied, thereby concealing any structural transitions that would otherwise produce shear-thinning effects [15]. Such modifications of the liquid structure can also influence the final amorphous state after vitrification. Indeed, previous studies have shown that shear deformation of metallic glass-forming liquids can alter local atomic packing motifs and produce rejuvenated glassy states with higher internal energy, even at similar cooling rates [16]. These observations suggest that even fully vitrified metallic glasses may exhibit significantly different local atomic structures and energy states depending on the thermal and mechanical history of the liquid prior to solidification.

Crystallization kinetics, and therefore the vitrification ability of Zr-based BMGs is also highly sensitive to the thermal history of the material in its liquid state before cooling. Key factors found in the literature include: stirring [17], overheating temperature [18], thermal cycling [17], and the initial microstructure of the alloy before melting [17]. In addition, chemical inhomogeneities and phase segregation have been reported when alloying Zr-based systems with refractory elements such as Nb, Ta, or Mo, particularly when the master alloy is prepared via direct arc melting of pure elements. This often results in incomplete mixing and uneven distribution. To mitigate these issues, a two-step alloying process is recommended, where the refractory element is first pre-alloyed with Zr before final arc melting [19,20]. Overall, these findings highlight the broad processing window and tunable vitrification parameters available for Vitreloy alloys, offering valuable opportunities to further enhance their GFA.

While the thermodynamic and thermophysical properties of Vit106a have been extensively characterized in the literature [9,10,13,15,21], its solidification behavior, particularly under varying processing conditions and at larger volumes remains comparatively underexplored. Previous reports demonstrating a remarkably low critical cooling rate of approximately 1.75 K s^{-1} were primarily based on small-scale samples, typically spherical specimens with diameters around 2 mm (30-45 mg). In contrast, the present study investigates the solidification dynamics of Vit106a in significantly larger volumes, employing spherical samples with a diameter of 6.5 mm (975 mg), representing more than a 30-fold increase in mass/volume. To gain deeper insights into the material's crystallization behavior and its sensitivity to processing conditions, solidification experiments were conducted using three distinct techniques: conventional arc melting under terrestrial conditions, and containerless electromagnetic levitation (EML) processing performed both during parabolic flights and aboard the International Space Station (ISS). The EML system was selected to eliminate container-induced heterogeneous nucleation, while the parabolic flights and ISS experiments provided access to short- and long-duration microgravity environments, respectively [22]. This study presents detailed observations of the crystalline phases and resulting microstructures following solidification, along with an in-depth analysis of how the thermal history of the liquid influences the supercooled liquid pathway upon solidification.

2. Experimental methods

2.1. Sample preparation

The Vit106a (nominal composition: $Zr_{58.5}Cu_{15.6}Ni_{12.8}Al_{10.3}Nb_{2:8}$) alloy samples were prepared using a two-step procedure [19,20], where a Ni–Nb prealloy was made with a composition Ni-74.27 wt% and Nb-25.76 wt%, which was then cast into 5 mm diameter rods. These rods were sectioned into precise weight slices for the final alloying step. For casting of the Vit106a alloy sample, ingot of 2.2 gr weight was produced by alloying Prealloy 1 with the elements Zr, Cu and Al. The alloy ingot was remolten several times to achieve homogenous composition. The sample was cast from the ingots into 6.50 ± 0.20 mm spheres (975 mg) in a water-cooled copper mold. The oxygen concentration measured via the LECO hot gas extraction method is ≤ 0.001 mass% (10 ppm), which is considered excellent for a Zr-based alloy. The actual surface composition was further analyzed by energy-dispersive X-ray spectroscopy (EDX) using a scanning electron microscope which matches closely with the nominal composition of $Zr_{58.5}$ $Cu_{15.6}Ni_{12.8}Al_{10.3}Nb_{2.8}$ [21].

2.2. Arc melting

The Vit106a alloy ingots were prepared by arc melting high-purity elemental metals (≥99.9%) in a water-cooled copper crucible under a high-purity argon atmosphere. Prior to melting, the chamber was evacuated to a base pressure of ~5 × 10^{-4} mbar and flushing by high purity Argon for several times. Afterwards, the arc-melter was filled by pure Argon (Ar 5.0, <2 vol.-ppm O_2) for the melting process. Additionally, a Ti getter was molten in the arc-melting furnace to further purify the atmosphere by reacting with residual oxygen before melting and suction casting of the Vit106a sphere.

2.3. Electro magnetic levitation (EML)

EML uses three non-contact instruments for scientific measurements and observation. A pyrometer, a video camera aligned with the coil's axis, and a high-speed camera positioned radially. Depending on the material and the environmental conditions, heating rates of up to 100 K s^{-1} can be achieved, enabling sample temperatures as high as 2100°C to be reached within 1 min. Both the heater and positioner voltages can be varied as linear functions of time. The digital pyrometer supports temperature measurements between 300°C and 2100°C, with a resolution of ≤ 0.1 K above 600°C. The pressure inside the two chambers can range from 10^{-8} to 400 mbar during experiments. Additionally, the EML gas distribution system allows for closed-loop gas circulation. This can be used to either apply a smooth gas flow onto the sample during the experiment or to flush particles and dust into a filter. A small nozzle integrated into the coil system enables the application of an adjustable gas flow onto the sample. This allows for controlled gas convection or a moderate increase in the cooling rate. The setup can use either vacuum, argon (Ar) or helium (He) for quenching, where the He flux provides the highest cooling rate [22].

2.4. X-ray diffraction (XRD)

XRD measurements were conducted in Bragg-Brentano geometry (θ-2θ) using an Empyrean diffractometer (Malvern Panalytical) equipped with a PIXcel3D-Medipix3 detector operating in line scan mode. The system was set to 45 kV and 40 mA, utilizing Cu-Kα radiation (combined $K\alpha_1$ and $K\alpha_2$). For structural analysis, a cross-sectional slice approximately 200 μm thick was extracted and scanned using X-ray diffraction in mapping mode to identify spatial variations in crystallinity. Measurements were taken at nine different positions across the sample, with relative displacements of ±2 cm in both the X and Y directions from the center. The X-ray beam had a footprint on the sample of approximately 20 mm^2. The amorphous content was calculated using the amorphous background subtraction method.

2.5. Wide-angle X-ray scattering (WAXS)

WAXS measurements were performed using a STOE IPDS II diffractometer with a MoKα radiation source ($\lambda = 0.71073$ Å) operating at 50 kV and 40 mA to analyze the overall sample quality and degree of crystallinity. Samples were mounted onto the goniometer head and positioned perpendicular to the X-ray and a 0.5 mm diameter beam was utilized in transmission mode. Diffraction patterns were captured on a 340 mm diameter image plate detection system positioned 200 mm from the sample with an exposure time of 120 min. Full diffraction images were recorded without sample movement, covering a 2θ range from 3° to 40°.

2.6. X-ray micro CT

Three-dimensional imaging was carried out using an RX Solutions EasyTom XL micro-computed tomography (μCT) system. A transmission-type X-ray tube was operated at 95 kVp and 50 μA, with a focal spot size of approximately 4 μm, for standard scans. The system featured a flat-panel detector with a resolution of 1880 × 1496 pixels and a pixel size of 127 μm, providing 16-bit grayscale depth for high dynamic range imaging. Depending on the region of interest, two voxel resolutions were employed: a global scan at 4.6 μm and local high-resolution scans with voxel sizes as small as 1.7 μm. The latter enabled to utilize appreciable edge-enhancement, *i.e.* phase contrast effects. For full-volume imaging, extended scans exceeding 12 h were performed using a reflection-type X-ray tube operated at 100 kVp and 90 μA, with a focal spot size of approximately 5 μm. A 0.5 mm aluminum prefilter was applied in this setup to minimize beam-hardening artifacts, achieving a final voxel size of 4.27 μm.

2.7. Image processing

The micro-CT images were used to segment the higher-intensity, fiber-like domains in the whole sample volume. Due to the very low contrast of these domains compared to the bulk of the material, conventional, simple segmentation methods were not applicable. This was further complicated by the defects and porosity present in the sample, which induced strong high-intensity artifacts around those regions. The artefacted pixel areas were mostly removed by grey-value thresholding and were excluded from further analysis. Subsequently, a machine learning-based 3D Trainable WEKA Segmentation 4.4 algorithm [23], a plug-in in the open-source software FIJI [24], was applied. The algorithm (random forest) was trained on approximately one-quarter of the full dataset to improve efficiency. The training features included mean, variance, Gaussian blur (blurring at different scales), derivatives (edges), and Hessian (for detecting elongated objects). The classifier algorithm was retrained through several manual iterations to improve performance. 3D renderings and visualizations of the micro-CT data were performed using the commercial software package VGStudio Max 3.5.

2.8. SEM imaging

The microstructural characterization of the samples was carried out using a field-emission scanning electron microscope (FE-SEM, ZEISS GeminiSEM 460) equipped with an Oxford Ultim Max 170 energy-dispersive X-ray spectroscopy (EDS) detector. SEM imaging for the EDS analysis was performed using the annular backscattered electron detector (BSD, 5 segments, ZEISS). Elemental mapping and compositional analyses were acquired and processed using the Oxford Aztec 6.0 software package. For point and ID analyses, a live acquisition time of 30 s was used. Elemental maps were collected with a pixel dwell time of 400 μs and a spatial resolution of 1024 × 1024 pixels.

3. Results

3.1. Earth sample- arc melting

The Vit106a sample produced on Earth was fabricated using conventional arc melting, followed by rapid cooling in a water-cooled copper mold (see Experimental Methods for details). While the exact quenching rate (Q_R) under these conditions is not directly measurable, it is estimated to lie within the range of 100 to 1000 K s^{-1} [2], significantly higher than the critical cooling rate of 1.75 K s^{-1} reported in the literature. The resulting sample shape is not perfectly spherical, as it adopted the shape of the copper mold, but its diameter is comparable to those produced under parabolic flight and on the ISS.

Fig. 1 presents the resulting XRD mapping patterns obtained after solidification. The sample is oriented to account for gravity, with the lower part corresponding to the south pole and the upper part representing the north pole (see little scheme in the middle). The sample is predominantly amorphous characterized by two broad humps centered around 2θ values of 37.5° and 64.5°. The amorphous percentage for each section is indicated above each graph, and it varies between 85% and 96%. Although the sample is predominantly amorphous, the presence of various crystalline phases is evident, which vary depending on the section of the sample that was scanned. Binary intermetallic phases of Zr–Al and Zr–Ni, specifically $ZrAl_3$ and Zr_2Ni, were identified, similar to those observed in our previous study on a fully crystalline Vit106a sample [21]. Interestingly, a monophase of cubic Nb was found in the southern part of the sample. The regions with the highest amorphous content are located in the central and northern parts of the sample, which were not in contact with the copper mold during processing. This suggests that the crystalline phases observed in the sample may be the result of static heterogeneous nucleation due to impurities on the container walls.

To gain a more localized understanding of the structure, we employed Wide Angle X-ray Scattering (WAXS) in transmission mode. The mapping was performed at five different locations on the sample: at the center and near the edges, including the North (N), South (S), East (E), and West (W) regions. The results are presented in Fig. 2 with the respective WAXS patterns obtained with the 2D detector, as well as the XRD diagrams generated by integrating the pattern along the azimuthal angle over 360°. Fig. 2(a) shows the 2D WAXS diagrams obtained from the northern, eastern, and central regions. The 2D WAXS diagram exhibits two broad diffuse rings, which are characteristic signatures of an amorphous phase. The corresponding 1D XRD patterns obtained by azimuthal integration from these three locations are identical and mainly present an amorphous signature. However, a small diffraction peak appears around $2\theta = 17.6°$ on the first amorphous halo. Upon closer inspection, additional low-intensity diffraction peaks emerge on the second amorphous halo, suggesting the presence of crystalline inclusions within the amorphous matrix. These investigated regions are estimated to consist of more than 95% amorphous matrix.

In contrast, the eastern region present in Fig. 2 (b) reveals a markedly different microstructure. The 2D WAXS diagram shows a polycrystalline structure with randomly oriented crystallites, and the 1D XRD pattern

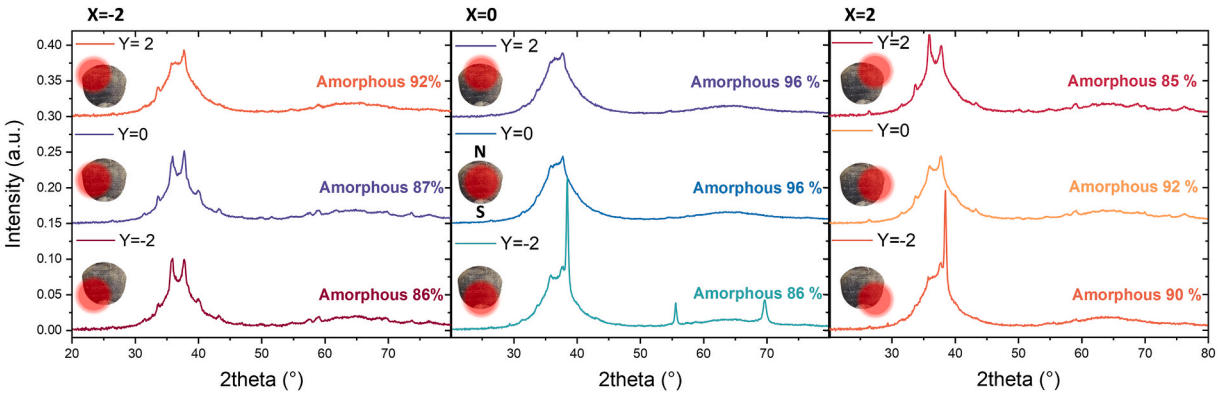

Fig. 1. – XRD patterns of the Vit106a sample produced by arc melting, collected at various locations across the specimen. A photograph of the sample is included in the figure, oriented with respect to gravity such that the south pole (S) points downward. The approximate 20 mm^2 irradiated by the X-ray beam is indicated for each measurement location. The XRD patterns have been normalized to account for differences in beam coverage. The sample is predominantly amorphous, and the estimated amorphous fraction is indicated above each corresponding pattern.

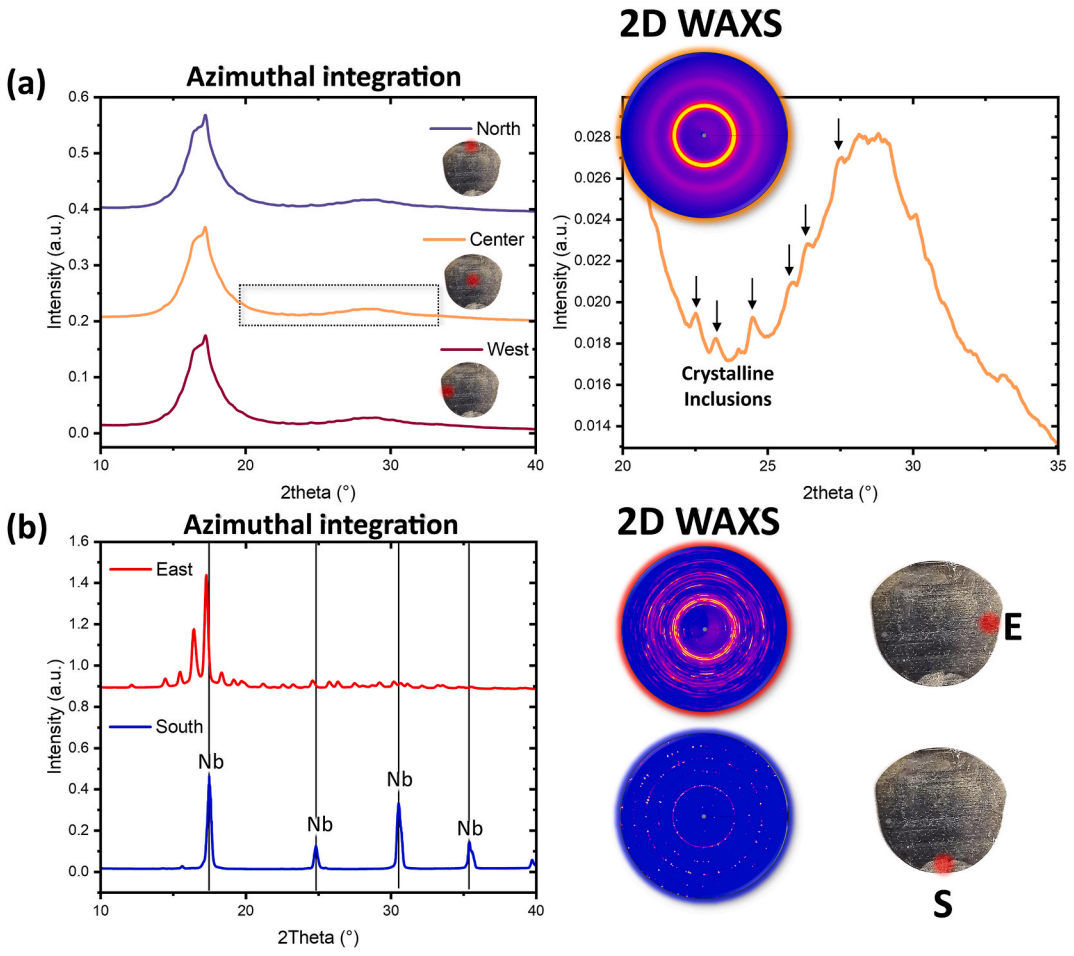

Fig. 2. **(a)** 2D WAXS patterns and corresponding 1D XRD profiles obtained via azimuthal integration from the center, north, and east regions of the sample. The data indicate a predominantly amorphous microstructure (~95%) with the presence of crystalline inclusions. **(b)** Similar analysis performed on the south and east regions of the sample reveals a fully crystalline structure. In particular, the southern region exhibits extremely large cubic Nb crystallites, attributed to gravity-driven sedimentation during solidification.

confirms a fully crystalline region with no detectable amorphous phase. Detected phases include tetragonal and hexagonal Zr–Al compounds, as well as a cubic Zr_2Ni phase. Notably, no Zr–Cu phase is present in this case [21]. Besides, most of the Nb appears to exist as a monophase instead as cubic $NbNi_2$ phase [21]. Indeed, the southern region shows discrete diffraction spots, indicative of extremely large crystallites. These reflections can be indexed as a cubic Nb phase. Interestingly, this phase separation is also visible macroscopically, distinguished by a lighter grey contrast on the sample surface.

The WAXS analysis reveals that the crystalline phases observed in the XRD mapping of Fig. 1 are highly localized and not uniformly distributed throughout the amorphous matrix. This strongly suggests that the

formation of large crystals is primarily driven by static heterogeneous nucleation on the container walls. In contrast, regions that were not in contact with the container exhibit a predominantly amorphous structure (over 95%). This indicates that, when contact-induced heterogenous nucleation is minimized the applied Q_R estimated to exceed 100 K s^{-1} is sufficient to suppress large-scale crystallization, but it may not be entirely effective in preventing nucleation on smaller scales since nano-crystalline inclusions are observed. Still, we cannot fully rule out the influence of static heterogeneous nucleation originating at the container walls and propagating into nearby amorphous regions. This highlights the importance of studying the vitrification mechanisms using container less techniques, which eliminate contact-induced nucleation sites. EML suspends a droplet of molten metal in vacuum using a magnetic field, entirely removing the influence of a mold or crucible. This approach enables a more controlled and uniform cooling process and offers a clearer insight into the intrinsic vitrification behavior of Zr-based BMGs.

3.2. Parabolic flight sample - EML

The second Vit106a sample is a 6.5 mm diameter sphere produced by EML aboard a parabolic flight. Parabolic flights offer a short-duration (approximately 20 s) microgravity environment comparable to that experienced on the ISS. In Fig. 3(a) and (b), the right-hand axis of the graph shows the acceleration experienced by the sample, where a value of 0 g corresponds to microgravity conditions. The diagram shows that the sample began heating once it was under microgravity conditions. The liquidus temperature (T_l) is indicated by the isothermal plateau observed at 1105 K, which aligns well with values reported in the literature for Vit106a [5,9,21]. The material was then heated to approximately 1530 K before being actively cooled using a helium (He) gas flow in an attempt to achieve vitrification. The Q_R from 1530 K to 1015 and 900 K is around 30 K s^{-1}, significantly higher than the critical cooling rate of 1.75 K s^{-1} reported for a 2 mm diameter Vit106a sphere [5]. Despite these conditions, an exothermic peak, commonly referred to as a recalescence plateau, appears at 1015 K during cycle 2, indicating the onset of crystallization even under microgravity conditions. In cycle 4, which corresponds to the final cycle, crystallization occurs under gravity at 900 K. Interestingly, a second exothermic peak is observed at a lower temperature of approximately 815 K, suggesting the occurrence of a secondary crystallization event or an additional phase transformation.

Fig. 3 (c) shows the temperature–time profile, illustrating the thermal history of the sample during cooling from the melt at 1530 K. In the first cycle, Argon (Ar) was used for cooling, resulting in a Q_R of approximately 17 K s^{-1}, and crystallization occurred at 1030 K. In the second and subsequent cycles, He gas was used, providing a higher Q_R of around 30 K s^{-1}, and the onset of crystallization is observed at 1015 K, whereas in the two following cycles crystallization occurred at lower temperatures, around 900 K. The variation in crystallization onset temperature across the four successive cycles indicates significant variability in the crystallization behavior.

Fig. 3(d) shows our cooling curve of cycle 2 superimposed on the Time-Temperature-Transformation (TTT) diagram developed by Hays et al. using ESL for the same Vit106a alloy but with a much smaller sample size. The TTT diagram was constructed using isothermal holds, in which the sample is rapidly cooled to a target temperature and maintained isothermally until crystallization (recalescence) is detected after a characteristic incubation time. We focus our analysis on cycle 2, since the presence of gravity in the other cycles may have promoted

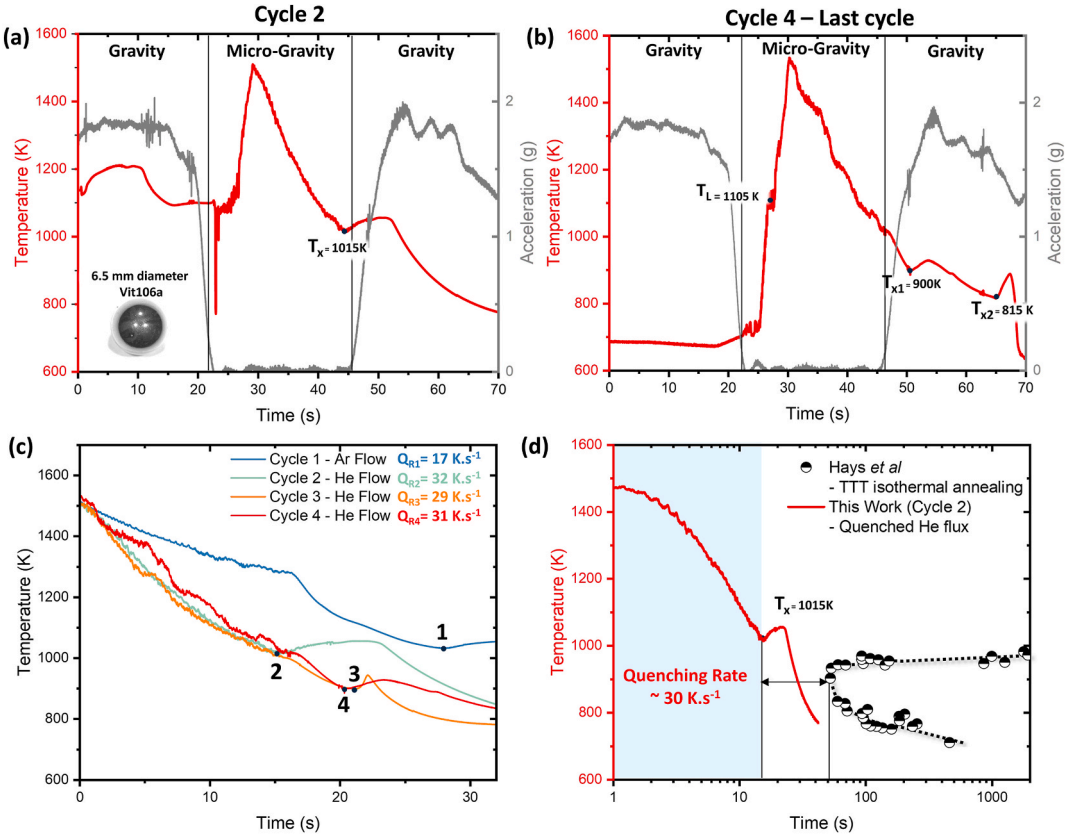

Fig. 3. (a)(b) Temperature–time profile of a levitated Vit106a droplet processed using Electromagnetic Levitation (EML) during a parabolic flight. Temperature was recorded with a pyrometer, while the right axis indicates the varying acceleration levels throughout the flight. Microgravity conditions, lasting approximately 20 s, are highlighted in the graph. **(c)** Four successive melting and solidification cycles of Vit106a performed during parabolic flight experiments showing variability in crystallization temperature. **(d)** Quenching curve of the sample overlaid on the Time-Temperature-Transformation (TTT) diagram established by Hays et al. [5] for a 2 mm-diameter Vit106a droplet. In our study, crystallization occurred significantly earlier than predicted, in a region where vitrification would typically be expected.

crystallization through contact with the sample holder, leading to heterogeneous nucleation (see Fig. S1). According to this TTT diagram, crystallization should not have occurred under the thermal conditions of our experiment.

WAXS mapping was also performed on the sample after cycle 4, as shown in Fig. 4. The XRD patterns obtained by azimuthal integration reveal that the material obtained after solidification is semi-crystalline, with the amorphous content ranging between approximately 0% to 40% depending on the sample region. This indicates that while crystallization occurred, the material remains partially amorphous, suggesting we are approaching the critical Q_R for this material and sample size. The WAXS patterns vary significantly depending on the scanned regions which demonstrate an heterogenous microstructure.

In Fig. 4(a), the WAXS patterns obtained in the center and north part display multiple diffuse and sharper rings. This indicates a semi-crystalline sample, with a polycrystalline structure with no preferential orientation with an amorphous matrix estimated to be comprised between 30 and 40%. However, in regions related to the East and West part, the diffraction rings appear partially discontinuous with different sizes, suggesting variations in crystal size across different areas of the sample. The West regions still show an amorphous matrix up to 30%, while the East part is almost fully crystalline. This implies a heterogeneous microstructure, where the degree of crystallinity and grain growth vary locally. All the diffraction peaks can be indexed to similar crystalline phases as those observed in the sample produced on ground by arc melting, namely, tetragonal Zr–Al intermetallics and a cubic Zr_2Ni phase. However, as on the earth sample the Zr_2Cu phase is not present while it was identified in our previous study on the ISS sample which is fully crystalline [21]. It is possible that this phase crystallizes following a lower cooling rate. Indeed, the Zr–Cu system show a very good glass forming ability for a broad composition range [25,26]. Although these crystalline phases are present throughout the entire sample, there is a small variation in the relative intensity of the diffraction peaks from one region to another, highlighting a small inhomogeneous distribution of the crystalline phases within the amorphous matrix.

Additionally, in the southern region of the sample, an isolated phase of cubic Nb is detected, which is completely distinct from the surrounding Vit 106a matrix (see S vs S–W in the graph), mirroring the behavior observed in the sample produced on Earth. The diffraction pattern from this region reveals exceptionally fine spots, indicative of large single crystal Nb phase. These diffraction spots are significantly sharper and more concentrated than those observed for the crystallites in the rest of the sample, suggesting that the Nb crystals in this region are much larger in size. Such phase separation is comparable to what has been observed on Earth in the southern region, where it can be attributed to gravity-driven sedimentation. A comparable phenomenon may have taken place in this case, as crystallization from the liquid state occurred after the end of the microgravity period, when the sample was once again subject to gravitational forces. It is plausible that the crystallization of this segregated phase is responsible for the second exothermic peak observed at 815 K. These findings also highlight a key limitation of using short-duration microgravity conditions (approximately 20 s).

3.3. ISS sample - EML

The final sample was produced aboard the ISS, which provides a long-duration microgravity environment, where thermophysical properties of the liquid state were measured during multiple melting–solidification cycles in Ref. [21]. During the parabolic flight, we observed significant variability in T_x over four melting–solidification cycles. Such variability in Zr-based BMG alloys has already been reported in the literature in similar ESL experiments but never deeply studied. Prior studies have noted a decrease in T_x with thermal cycling [17,18], a sharp drop in T_x when a certain overheating threshold is exceeded [18], and the influence of the alloy's initial microstructure prior to melting [17]. All of these factors contribute to the variability in crystallization behavior. The most critical parameter reported so far is the overheating temperature (T_{OH}) [18]. The overheating temperature T_{OH} is defined as the maximum temperature reached above the melting point prior to quenching.

Consequently, we examined the different cooling profiles of Vit106a

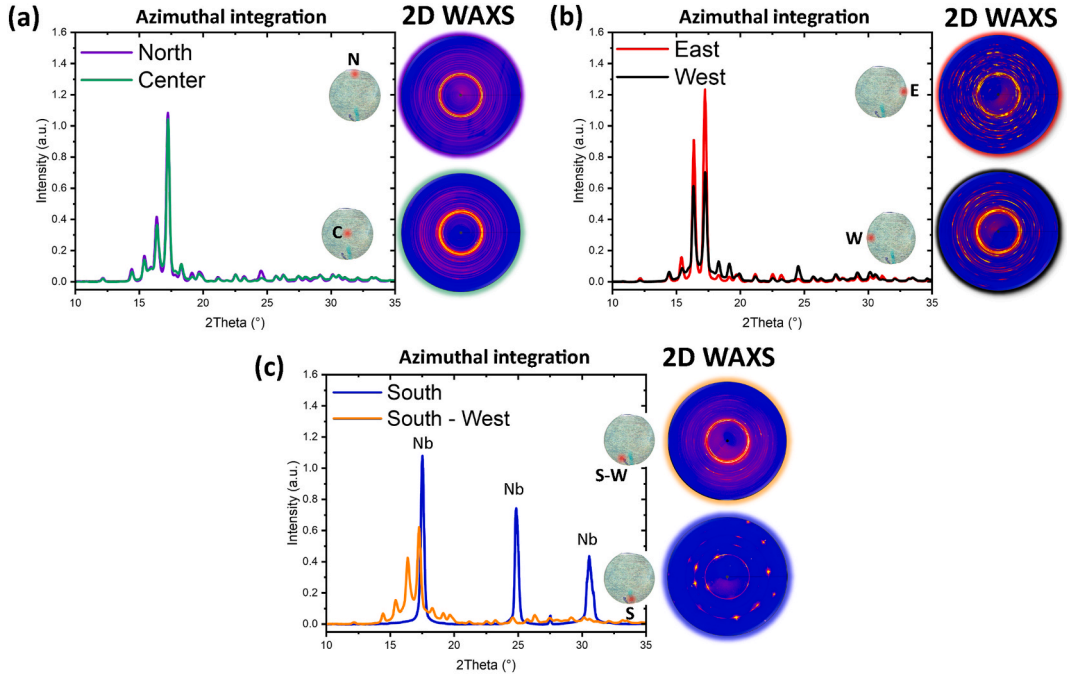

Fig. 4. 2D WAXS pattern mapping and corresponding 1D XRD profiles obtained via azimuthal integration from the center, north, east, and west regions of the sample. **(a)(b)** 2D WAXS images reveal a semi-crystalline matrix with a polycrystalline structure, characterized by randomly oriented grains and variations in both the amorphous phase fraction and crystallite size. **(c)** The diagrams on the bottom part show data from the south and adjacent southwest (S–W) regions of the sample. In the southern region, discrete diffraction spots indicate the presence of very large crystals of cubic Nb, suggesting gravity-induced phase segregation.

liquid droplets obtained under various experimental conditions used to measure thermophysical properties (see Fig. 5). These include: **(a)** standard heating and cooling experiments for solidification study using a single heating voltage pulse; **(b)** the oscillation droplet method for viscosity (η) and surface tension (σ) measurements, where the sample is subjected to multiple short excitation pulses during cooling prior to quenching, and; **(c)** Modulation used for emissivity (ε) and specific heat capacity (c_p) measurements, which involve a sinusoidal temperature modulation with short and longer frequency applied during the cooling phase prior to quenching.

This statistical analysis carried out over 60 thermal cycles enables the identification of reproducible trends across cycles and helps to determine which parameters have the most significant influence on the supercooled liquid state. It is important to note that the cycle numbers are identifiers rather than chronological indicators. For example, cycle 35 shown in Fig. 5 (a) corresponds to the first thermal cycle applied to the sample. Besides, the Q_R is not constant during cooling, it is higher at the beginning of the cooling process when the temperature is still high, and decreases as the sample approaches T_x, as shown by the Q_R versus time profile in Fig. S3. Consequently, in each graph, the range of Q_R values is explicitly indicated, with the lowest Q_R value corresponding to the value near T_x.

In Fig. 6(a)(b)(c), we present successive heating–cooling cycles performed using a single heating pulse to investigate solidification behavior under identical conditions (*i.e.*, same T_{OH} and Q_R). It seems there is a small decrease of T_x with thermal cycling. Notably, in cycle 59, crystallization occurs at a lower temperature ($\Delta T_x = -10$ K) than in cycle 58. A similar trend is evident in cycles 76–79: T_x gradually decreases from cycle 76 to 78, but remains constant between cycles 78 and 79, suggesting a cumulative but saturating effect. The summary plot on the right illustrates this effect, revealing a drop in T_x of approximately 8–12 K with repeated cycling, which is a relatively small variation.

Fig. 6 (d)(e)(f) illustrates the effect of varying convective Ar gas flow rates (ranging from 0 to 4 L/min) on successive thermal cycles. The use of an inert gas flux enhances both the Q_R and thermal homogeneity of the cooling process. Between cycles 66 and 68, increasing the Ar flow rate results in a rise in the Q_R from 17.5 to 7.0 K s^{-1} to 21.5–9.0 K s^{-1}, accompanied by a significant reduction in T_x of approximately 80 K. Interestingly, although the change in quenching rate between cycles 67 and 68 is relatively small, T_x decreases markedly, suggesting a possible synergistic effect between thermal cycling and enhanced convective cooling. A similar trend is observed between cycles 72 and 75, although these are not consecutive, indicating that the reduction with convective flux is not limited to sequential cycling.

In the next stage, we investigated the effect of increased T_{OH} on successive thermal cycles, using either a single heating pulse or the oscillating droplet method (see Fig. 7(a)(b)). Cycles 35 to 37, which were the first thermal cycles of the batch, employed a single heating pulse with He-assisted quenching, yielding the highest Q_R of the batch with Q_R ranging from 45 to 17.5 K s^{-1}. When the T_{OH} was increased by 150 K, the T_x decreased by approximately 15 K. A similar trend is observed for cycle 58-59 and 60-61. For cycle 58-59 the T_{OH} is 1600 K and T_x is around 1005 K, while for cycle 60-61 the T_{OH} is around 1485 K and T_x is around 1020 K (see Fig. 6(a)(c)).

Additionally, although the Q_R in cycles 35-37 was significantly higher than in cycles 66–68, the samples crystallized at a higher temperature likely because these were the first cycles of the batch and had not yet accumulated thermal cycling. For instance, in the sample processed during the parabolic flight, cycle 2 of the batch (using He-quenching) crystallized at 1015 K, while crystallization occurred at 900 K in the subsequent cycles (3 and 4) under the same conditions (see Fig. 3 c). This indicates that the effect of thermal cycling may be more pronounced in the first cycle of a batch. Gangopadhyay et al. also note that they routinely exclude the first cycles from statistical analysis, as their Vit106 samples tend to crystallize at higher temperatures during these initial cycles [17]. However, in the case of cycle 35-37, the recalescence plateau is significantly less pronounced compared to later cycles in the batch, suggesting that the sample remains partially amorphous due to the elevated Q_R. By contrast, in cycles 18 to 20, where the oscillating droplet method was used, an increase in T_{OH} by 150 K resulted in a much larger decrease in T_x of about 35 K. Notably, in this set, cycle 20 exhibited a significant higher T_x compared to cycle 18 opposite to the effect expected from thermal cycling alone.

Finally, we investigated the effect of thermal modulation applied in different temperature ranges. This was carried out in cycles 1 to 4, where only modulation was applied (the corresponding experimental parameters are summarized in Table S1). The temperature ranges referred to as "High T″ range spanned from 1235 K to 1550 K, while the "Low T″ range corresponds to modulation between 1100 K and 1275 K. The results indicate that modulation has a pronounced impact, as evidenced by a substantial 80 K shift in T_x between the High T and Low T conditions even for very low Q_R of around 2 K s^{-1}. This highlights the strong sensitivity of nucleation behavior to thermal history using modulation within specific temperature windows.

The last melt-solidification cycle was conducted three years later, just before the sample was returned to Earth from the ISS (see Fig. S4 in Supporting Information). During this cycle, crystallization occurred at 1035 K. Fig. 8 (a) Shows the 2D WAXS patterns reveal a polycrystalline structure with randomly oriented crystallites. The diffraction rings are characterized by fine, well-defined spots, indicative of a large crystallite size. These spots appear significantly finer than those observed in the parabolic flight sample, which reveals a larger crystallite size for the ISS sample. No notable differences are visible in the 2D patterns between the four examined positions (North, South, East, and West). However, the XRD profiles, obtained through azimuthal integration, display clear variations. While all regions exhibit similar diffraction peaks,

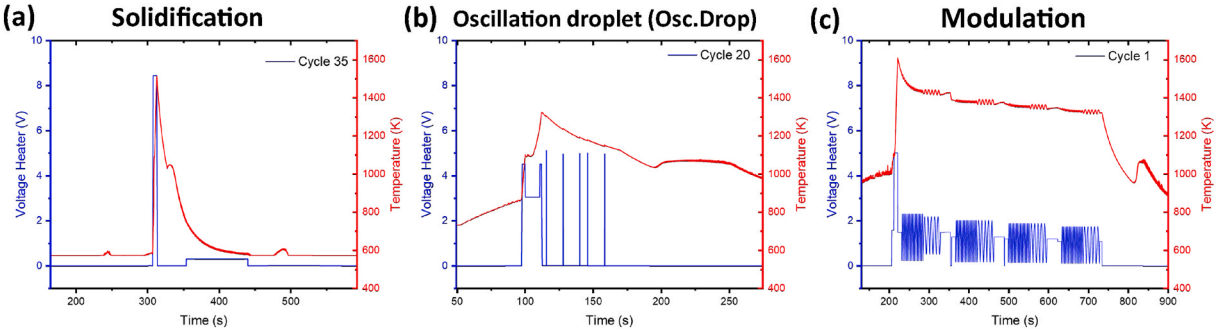

Fig. 5. Time evolution of the heater voltage (blue) and the surface temperature of the Vit 106a sample measured by a pyrometer (red) during different melting–solidification cycles used to assess the thermophysical properties of the liquid state.**(a)** A single heating pulse is applied to melt the sample, followed by passive cooling upon power shutoff.**(b)** For viscosity (η) and surface tension (σ) measurements, short excitation pulses are applied during the undercooling.**(c)** A sinusoidal voltage modulation is applied during undercooling to extract specific heat capacity (c_p) and emissivity (ε).

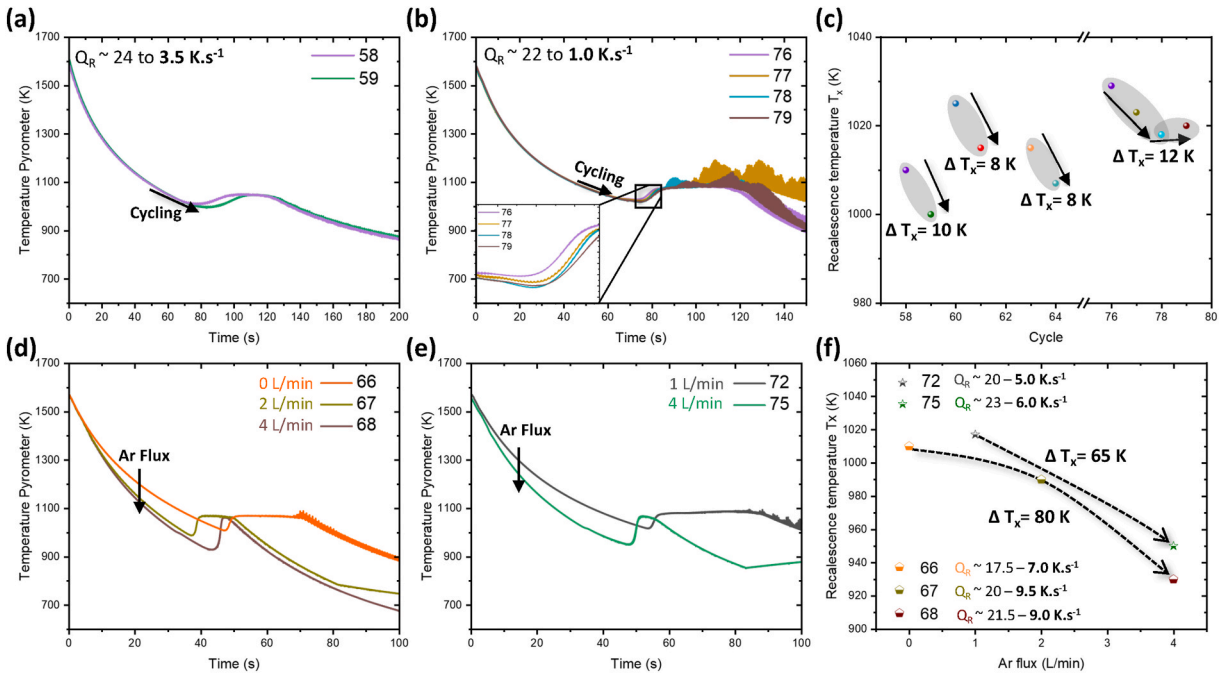

Fig. 6. – Temperature–time profiles from various cooling cycles of liquid Vit106a droplets processed using electromagnetic levitation (EML), illustrating the influence of the thermal history on nucleation behavior. **(a)(b)(c)** Effect of repeated cycling under identical processing conditions, showing a slight decrease in the crystallization temperature T_x of approximately 8-12 K with repeated identical cycles. **(d)(e)(f)** Influence of convective argon (Ar) gas flow on quenching efficiency and crystallization behavior. Increased Ar flow enhances the cooling rate, resulting in a further reduction in T_x.

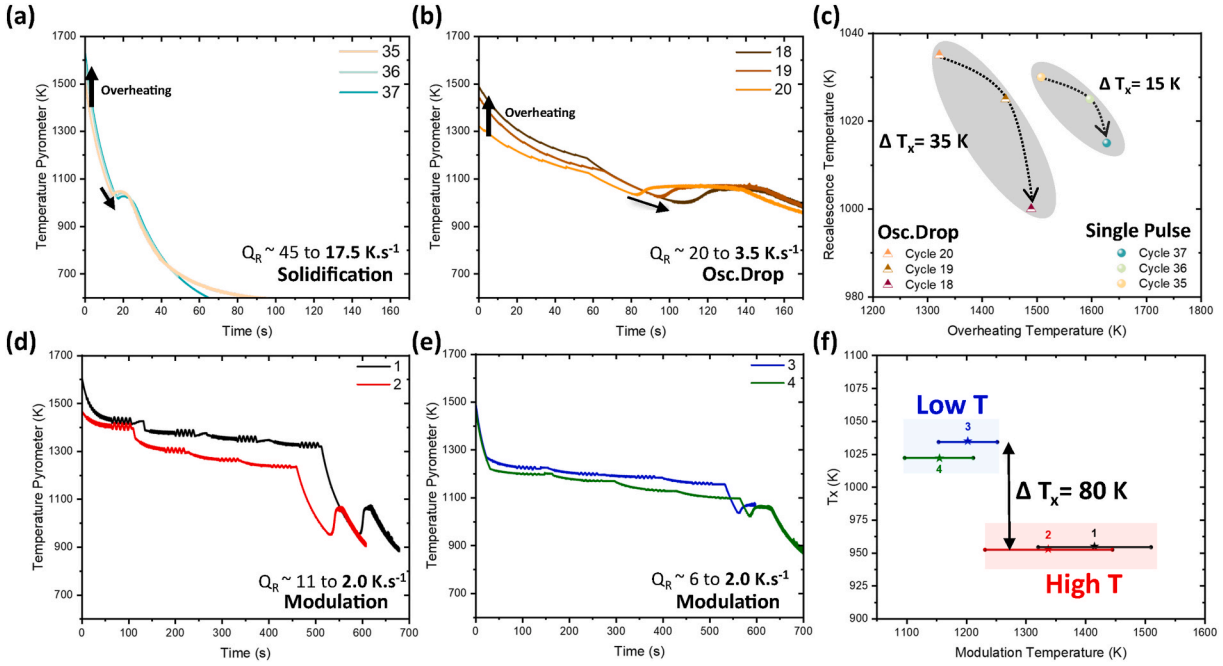

Fig. 7. – Temperature–time profiles from various cooling cycles of liquid Vit106a droplets processed using electromagnetic levitation (EML), illustrating the influence of the thermal history on nucleation behavior. **(a)** Influence of the overheating temperature on T_x, using standard heating-cooling cycle and **(b)** using oscillation droplet measurements involving short excitation pulses during undercooling. **(c)** Comparison of the overheating dependence of T_x for standard heating–cooling cycles and oscillating-drop experiments. Although both processing conditions lead to a reduction in T_x, the effect is significantly more pronounced during oscillating-drop measurements. **(d)** Thermal modulation applied in the high-temperature range (1550–1235 K). **(e)** Thermal modulation applied in the lower temperature range (1275–1100 K). **(f)** Influence of modulation applied over different temperature intervals on the crystallization behavior of Vit106a. Modulation performed in the high-temperature range (strictly above 1250 K) results in a significant reduction in the crystallization temperature T_x (up to 80 K), even at very low quenching rates, suggesting the existence of a critical temperature threshold above which the thermal history strongly modifies the nucleation pathway.

confirming the presence of the same crystalline phases in all those regions, their relative intensities vary markedly. Certain reflections show low intensities in some regions and much higher intensities in others, indicating a small inhomogeneous distribution of crystalline phases within the sample. Quantitative analysis of XRD mapping reveals pronounced heterogeneity in the spatial distribution of crystalline domains.

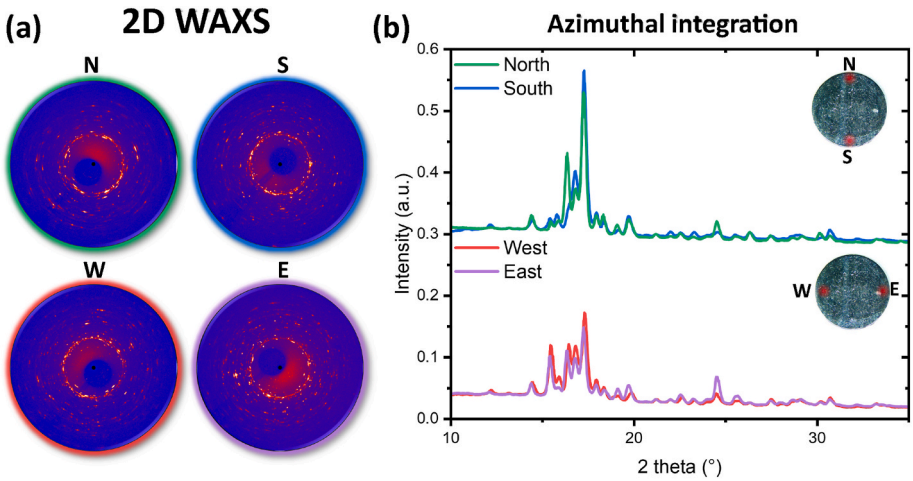

Fig. 8. – **(a)** 2D WAXS patterns and **(b)** their corresponding azimuthal integrations, recorded at different positions on the sample cross-section: North (N), South (S), East (E), and West (W). The WAXS patterns exhibit small, randomly distributed diffraction spots, indicative of a polycrystalline structure composed of randomly oriented, large crystallites. Unlike the sample produced during the parabolic flight, no significant variation in spot size is observed across different regions.

Large crystalline regions impose inhomogeneous strain on neighboring crystalline phases within the same area (see Fig. S6). This mapping further shows that the tetragonal Zr_2Cu phase is relatively homogeneously distributed, as evidenced by the consistent integrated intensity of diffraction peak 4 (see Fig. S6) across the scanned regions in both XRD and WAXS measurements. In contrast, diffraction peak 3, associated with the cubic Zr_2Ni phase, exhibits substantial spatial variations in intensity, indicating localized enrichment or depletion of this phase.

The microstructure and spatial distribution of crystalline phases within the cross-section of the sample were analyzed using a combination of scanning electron microscopy (SEM) and phase-contrast X-ray computed tomography (XCT), as presented in Fig. 9. The sample exhibits a notable degree of open porosity, predominantly located in the central region, while closed porosity is more uniformly distributed throughout the volume, ranging from approximately 4×10^{-5} to 4×10^{-4} mm^3. Within the open porous regions, SEM imaging reveals a complex microstructure composed of two main types of crystalline domains. Highly anisotropic, fiber-like domains, extending up to 200 μm in

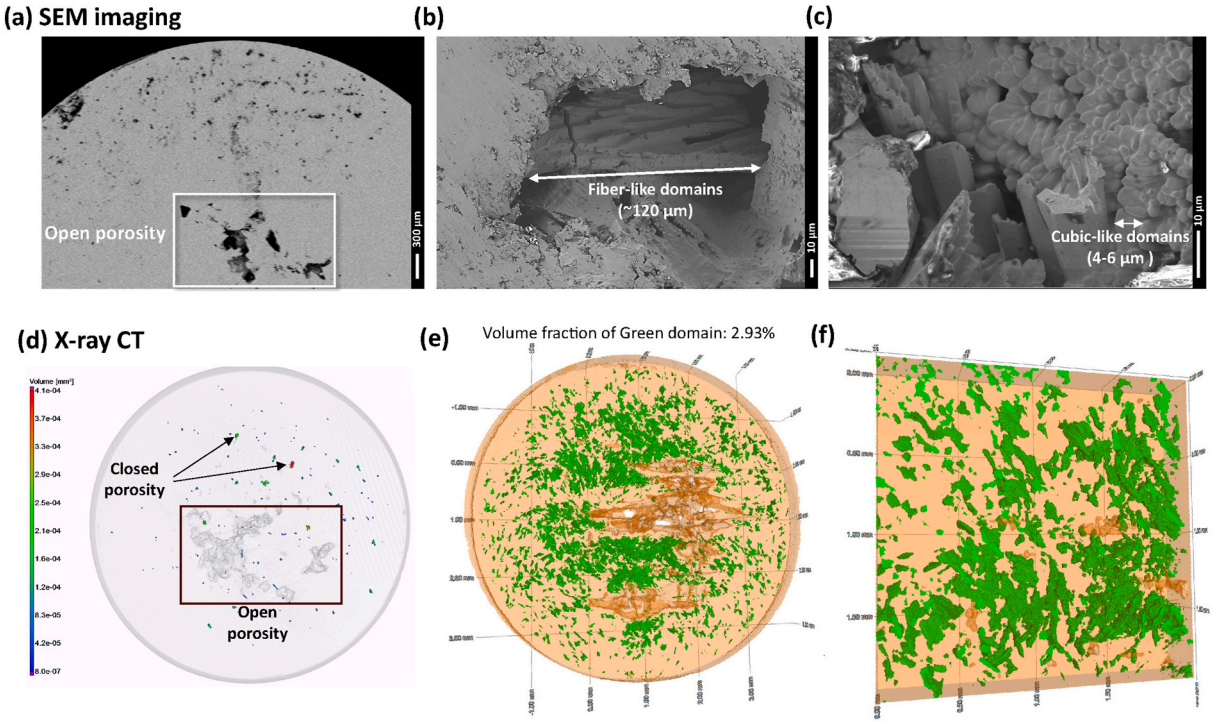

Fig. 9. **(a)** SEM images of the cross-section of the Vit106a sphere, revealing significant open porosity concentrated near the center. The largest voids expose internal microstructural features, **(b)** including elongated, fiber-like crystalline domains reaching lengths of up to 120 μm, **(c)** as well as smaller, more equiaxed domains approximately 4–6 μm in size. **(d)** 3D rendering of X-ray attenuation micro-CT of the sample with the material made 80% semi-transparent thus highlighting both open and closed porosity (the closed porosities being color coded according to their size). **(e)-(f)** 3D reconstruction of the segmented fiber-like crystalline domains (colored green), the right most obtained using the local, high-resolution phase-contrast X-ray micro-CT. These domains account for an estimated 2.93% of the total sample volume. Note that the defects shown in the 3D rendering in the middle figure of the micro-CT in the middle of the sample (in the black rectangle on the left side image) are artificially enlarged due to excluding surrounding regions from the analysis that are highly influenced by artifacts (see Methods, Image processing).

length, are observed alongside smaller, more equiaxed domains with typical dimensions of 4–6 μm. The elongated domains are attributed to orthorhombic or tetragonal Zr–Al phases and tetragonal Zr_2Cu, while the smaller, symmetric domains likely correspond to cubic Zr_2Ni and Nb_2Ni phases. Due to their large dimensions, the fiber-like domains are resolvable using phase-contrast XCT, enabling segmentation and volumetric analysis across the entire scanned volume. In contrast, the smaller domains fall below the voxel resolution (voxel size = 4.7 μm) and cannot be individually distinguished by X-ray imaging. The segmented volume fraction of the fiber-like crystalline domains is estimated to be ~3%. Their spatial distribution is slightly inhomogeneous, with a higher concentration near the sample center compared to the edges.

4. Discussion

For the samples produced on earth and on parabolic flight, a region in the lower part of the sample contains large Nb crystals, indicating that Nb was not uniformly incorporated into the amorphous/crystalline matrix. This issue has previously been reported by Fan et al., who observed isolated micrometer to millimeter-sized Nb-rich phases in Vit106a, which led to enhanced ductility of the alloy upon deformation [19,20]. The segregation was attributed to the incomplete melting of Nb, likely due to the substantial difference in melting points between Nb (T_m = 2742 K) and the other constituent elements. Additionally, the higher density of Nb ($\rho = 8.6$ g cm^{-3}) compared to most Zr-based bulk metallic glasses (approximately ρ = 6.5 g cm^{-3}) contributes to gravitational segregation of the refractory elements during melting.

To address this issue, Fan et al. employed a two-step synthesis method in which a Zr–Nb pre-alloy was first prepared and subsequently arc-melted with the remaining elements [19,20]. This approach allowed for more homogeneous incorporation of Nb into the matrix. Similarly, in our study, the three Vit106a alloys were also prepared using a two-step process, in which a Nb–Ni pre-alloy (Ni_3Nb $T_m = 1400$ K) [27] was first synthesized and then combined with the other constituents. However, in our case, large Nb-rich regions were still observed in the lower part of the sample. The SEM–EDX mapping (see Fig. 10) performed on the segregation zones of both the Earth-processed sample and the parabolic-flight sample primarily reveals Nb-rich regions containing isolated subdomains enriched in Ni, Zr, Cu, and Al. This observation suggests that Ni is preferentially associated with the Zr–Cu–Al-rich matrix rather than remaining chemically associated with Nb after solidification. This suggests that although the Nb–Ni pre-alloy had successfully melted, Nb subsequently segregated during the post-processing solidification stage, likely under the combined influence of gravitational effects and limited atomic redistribution in the liquid state. This behavior can be attributed to the relatively weak chemical interactions of Nb with several alloy constituents, particularly Cu ($\Delta H_{mix}(Nb-Cu) = +3$ kJ/mol) and Zr ($\Delta H_{mix}(Nb-Zr) = +4$ kJ/mol) [28,29], which promote the formation of Nb-enriched residual regions rather than complete incorporation into the surrounding matrix. Although Nb can form stable Nb–Ni intermetallic compounds ($\Delta H_{mix}(Nb-Ni) = -30$ kJ/mol), the relatively low Ni concentration in Vit106a (~12 at. %) together with the stronger affinity of Ni for Zr ($\Delta H_{mix}(Zr-Ni) = -49$ kJ/mol) likely limits the amount of available Ni capable of stabilizing Nb-containing phases, thereby further promoting

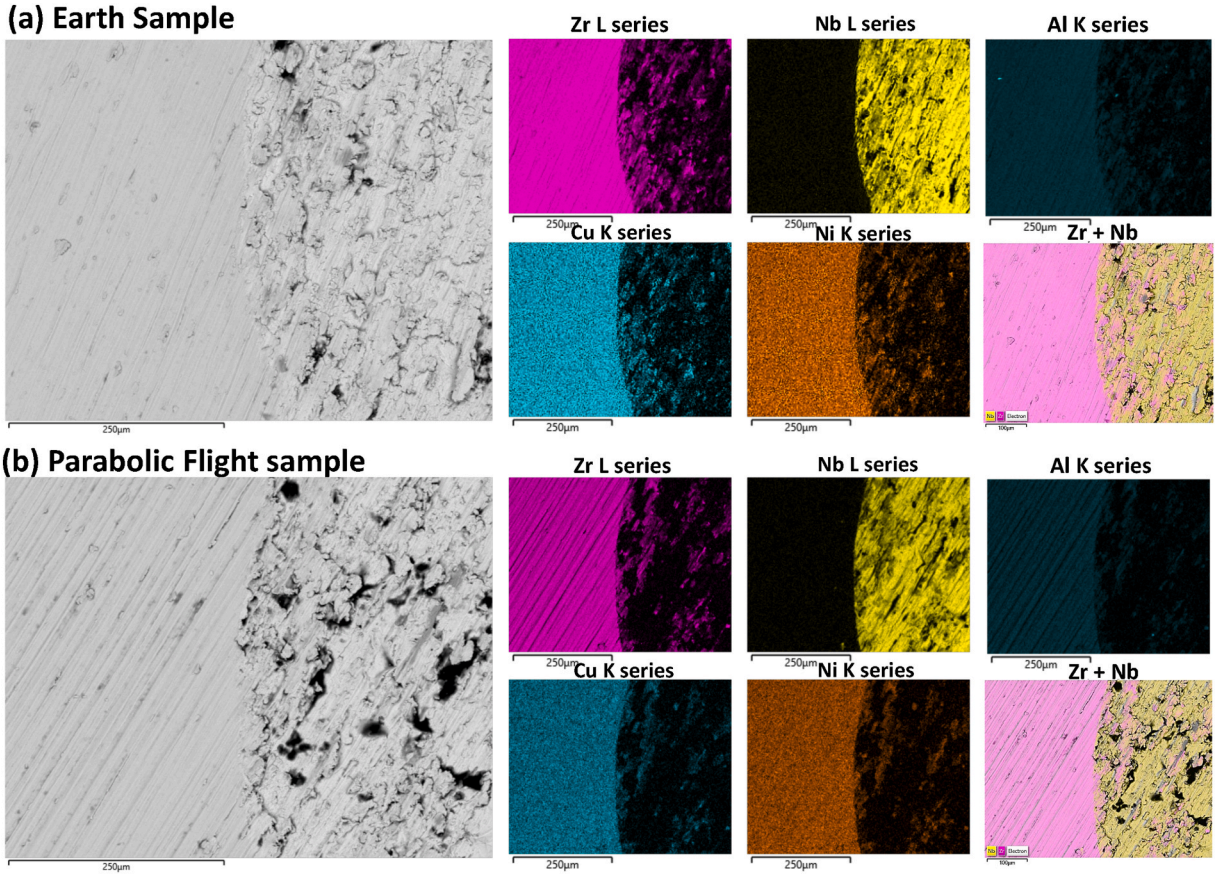

Fig. 10. –SEM micrographs and corresponding EDX elemental maps obtained from two Nb-rich segregated regions observed **(a)** in the Vit106a sample processed by arc melting on earth and **(b)** in the Vit106a sample processed by EML in the parabolic flight. For each region, the left image shows the SEM micrograph, followed by the elemental distributions of Zr (magenta), Nb (yellow), Cu (cyan), Ni (orange), and Al (dark blue), together with the combined layered EDX map. The Nb-rich domains exhibit a strong enrichment in Nb while containing smaller isolated regions enriched in Zr–Cu–Ni–Al components. These observations indicate that the segregated regions are predominantly Nb-rich rather than fully pure Nb.

Nb segregation.

This suggests that gravity-assisted redistribution may occur during liquid-state processing. Using the liquid viscosity values previously measured for Vit106a [21], together with a simplified Stokes settling estimation, we can deduce that the sedimentation velocity strongly depends on the characteristic size of the Nb-enriched domains (see supplementary section- Stokes settling estimation for Nb-rich domains). For nanoscale clusters (10–100 nm), the calculated displacement during the typical melt residence time remains negligible (<0.1 μm). In contrast, micron-sized Nb-rich liquid domains (1–50 μm) can theoretically travel distances ranging from several tens of micrometers up to millimeters depending on their size (see Table S2).

These calculations indicate that the observed segregation is unlikely to originate from atomic-scale sedimentation of individual Nb atoms in a fully homogeneous liquid. Instead, the results support a mechanism involving liquid-state compositional heterogeneities in the form of large Nb-enriched liquid domains, followed by gravity-assisted redistribution during cooling and solidification. Such behavior is consistent with the relatively weak chemical affinity of Nb with several alloy constituents. Interestingly, this phase segregation is not observed in the ISS sample produced under microgravity conditions. In this case, Nb appears to be incorporated more homogeneously into the matrix, with the formation of a cubic Nb_2Ni phase. However, the ISS sample was also subjected to transient thermal modulation during cooling, which may have influenced elemental redistribution and mixing within the liquid. Therefore, it cannot be concluded that the improved Nb incorporation originates solely from microgravity conditions. Although Nb segregation was observed in the Earth and parabolic-flight samples, it is possible that the thermal modulation enhanced liquid mixing and promoted chemical homogenization, thereby limiting phase segregation during solidification. Overall, the observed Nb-rich regions likely originate from coupled liquid-state mechanisms involving Nb-enriched domain formation and gravity-assisted redistribution during processing.

The Vit106a sample produced by arc melting also shows a heterogeneous distribution of intermetallic crystalline phases at its edges. This suggests that crystallization starts locally, likely at the container walls. In contrast, a Vit105 sample of the same size and processed under the same conditions remains fully amorphous throughout its volume, even though its critical quenching rate is five times higher (10 K s^{-1}) than that of Vit106a (see Fig. S7). Oxygen is unlikely to explain this behavior, as the Vit106a sample contains very little oxygen (<10 ppm), even less than our Vit105 sample (<80 ppm). These observations indicate that Vit106a is highly sensitive to heterogeneous nucleation. This is further supported by another study, where Vit106a cooled at 3–4 K s^{-1} in a graphite crucible crystallized at 1075 K instead of 900-950 K, while Vit1 showed no recrystallization under the same conditions [15]. Although this sensitivity is detrimental when attempting to obtain a fully homogeneous amorphous phase, it may also offer opportunities for the development of bulk metallic glass composites (BMGCs). Indeed, controlled crystallization within an amorphous matrix is known to improve ductility and toughness through the suppression, branching, or deflection of shear bands. Recent studies on Ti-based BMGCs containing ductile β-Ti dendrites have demonstrated significantly enhanced tensile ductility, work hardening, and fracture toughness compared to monolithic metallic glasses due to the interaction between crystalline phases and propagating shear bands [30,31]. Consequently, such materials could potentially be engineered by introducing selected heterogeneous nucleation sites and carefully controlling the cooling conditions in order to tune the size, distribution, and fraction of crystalline phases within the amorphous matrix, similarly to the partially crystallized structure observed in the sample produced during the parabolic flight.

Regarding the vitrification of Vit106a under levitation, a critical Q_R of ~2 K s^{-1} was reported in ground-based experiments using ESL for a 2 mm diameter Vit106a sphere [5]. However, this value differs significantly from what we observed in our experiments using a much larger Vit106a sample (~30 times greater in mass/volume). A heterogenous nucleation process may be at play within the supercooled liquid and could explain this crystallization kinetics disparity. This is supported by post-solidification analyses of Vit106a samples processed aboard the ISS and during parabolic flights, which exhibit subtle microstructural heterogeneities. These include spatial variations in crystallinity, crystalline phase distribution, crystallite size and strain, as revealed by XRD/WAXS and X-ray μ-CT analysis. In multicomponent alloys like BMGs, the solidification process is governed by a complex interplay between liquid-state behavior and nucleation/growth phenomena, making it difficult to pinpoint the exact mechanisms involved [32]. Such heterogeneous structures may arise from dynamic heterogeneities within the bulk liquid, such as localized temperature and atomic mobility gradients [33], liquid-composition inhomogeneities, spinodal decomposition phenomena [34–36], or nanoscale structural clustering [37,38]. As the sample volume increases, the likelihood of dynamic heterogeneities acting as preferential nucleation sites within the liquid also rises, highlighting the need for careful process optimization, particularly for larger-scale samples and complex alloys [2].

For example, a 6.5 mm diameter Vit105 sphere sample was successfully vitrified aboard the ISS during several heating–cooling cycles at a quenching rate Q_R of ~11 K s^{-1} [39]. However, in other cycles, the same sample crystallized despite a higher Q_R of ~16 K s^{-1} and a higher T_{OH} (see Fig. S8). Similarly, in a study by Gangopadhyay et al. on a 6 mm diameter Vit106 sphere, vitrification was achieved only in one cycle and could not be reproduced under similar Q_R conditions. Although the underlying reason remains unclear, this demonstrates that the GFA of these Zr-based alloys cannot be defined solely by a critical Q_R. Instead, it strongly depends on processing conditions, which can be optimized to achieve vitrification.

Without specific processing optimization, the critical Q_R of Vit106a appears to exceed 30 K s^{-1}, as the sample produced during the parabolic flight was partially amorphous (up to 40%) and crystallized at the temperature corresponding to the "nose" of the TTT diagram ($T_x = 900$ K). For samples processed on the ISS, we observed a huge variability and a strong dependence of T_x on the liquid thermal history over 60 thermal cycles, with T_x ranging from 930 K up to 1035 K. The lowest crystallization temperature range of 930-950 K corresponds to the upper temperature part of the TTT diagram (see Fig. 3(b)) and was reached under certain processing conditions. We found that several factors significantly affect crystallization behavior, including thermal cycling, inert gas convective flux, and particularly oscillation drop technique and sinusoidal temperature modulation coupled with overheating temperature. The most effective approach for reducing T_x was either increasing Ar flow (higher quenching rate) or the application of thermal modulation coupled with high T_{OH}.

The influence of T_{OH} on the stability of the supercooled liquid state suggests that the liquid undergoes changes in its thermophysical and/or structural properties with temperature. Interestingly, the observed sharp drop in the supercooled liquid region ($\Delta T_x \approx 80$ K) observed even for very low cooling rate (2-3 K s^{-1}) under temperature modulation, indicates that above a certain threshold temperature the liquid experiences a significant transformation, which in turn affects the extent of the supercooled liquid regime. Premature crystallization observed in levitation techniques when processing Zr-based BMG is usually attributed to heterogeneous nucleation triggered by impurities or elevated oxygen content within the sample [18,40]. Indeed, Lin et al. and Mukherjee et al. suggested that the effect of T_{OH} on the supercooled region is due to the dissolution/melting of the impurity nucleation site within the liquid above a certain temperature.

However, the oxygen content measured in our sample was found to be very low in pre-flight measurement (~10 ppm). Besides, if contamination were the dominant factor, one would expect only ΔT_x being dependent on T_{OH}. In contrast, we observe only a relatively small T_{OH} effect when using conventional heating and cooling protocols, which does not support the hypothesis of impurity dissolution above a certain temperature. One possible explanation is that the time spent within the

relevant temperature range during heating and cooling is insufficient to fully dissolve oxide clusters. Although melting itself is generally rapid, the dissolution of stable oxide particles can remain kinetically limited due to the sluggish atomic diffusion and low chemical reactivity of refractory oxide species in metallic melts. Nevertheless, this interpretation remains questionable, since even at temperatures as high as 1650 K the T_{OH} effect remains moderate during heating and cooling. Therefore, it may be possible that another mechanism is involved in enhancing the stability of the supercooled liquid state. Notably, the T_{OH} effect becomes much more pronounced when using the oscillating drop technique and temperature modulation, but only above approximately 1300 K.

Some structural transitions in the liquid state of Vit alloys have been widely reported in the literature in this temperature range, which in turn influence their thermophysical properties [6–13]. They are often revealed by exothermic events in specific heat capacity (C_p) curves during cooling [6–8]. This structural transition is frequently associated with a fragile-to-strong liquid transition, evidenced by a marked change in the temperature dependence of viscosity. For Vit106a, exothermic peaks indicative of a liquid structural disordered-to-ordered transition have been observed in C_p/ε curves between 850 K and 900 K in the undercooled liquid [7,41]. A detailed structural investigation on a Vit1 alloy revealed a pronounced thermal hysteresis in this structural transition [6,8]. During heating, the ordered-to-disordered liquid transformation occurs above 1150 K, whereas during cooling, the reverse transition (disordered-to-ordered) takes place near 800 K. Furthermore, studies have shown that the ordered-to-disordered transition in Vit1 is strongly influenced by shear forces applied to the liquid during heating [14]. Under applied shear at 1075 K, the viscosity decreases by nearly one order of magnitude. At temperatures above 1225 K, this effect becomes even more pronounced, with viscosity dropping by two orders of magnitude. Beyond this point, the liquid behaves as a fully Newtonian fluid, exhibiting no observable shear-thinning at higher temperatures. In contrast, in the absence of shear, the viscosity did not drop, and this ordered-to-disordered transition may not occur at all. Instead, the liquid retains a high viscosity, up to two orders of magnitude greater, across the 1000–1200 K temperature range [14]. These observations underscore the significant influence of both shear and overheating on the liquid's viscosity behavior of Vit alloys, and therefore on the potential impact on the subsequent solidification upon cooling.

In our case, the application of sinusoidal temperature modulation to the liquid state induces temperature gradients that cause periodic expansion and contraction, generating density fluctuations that drive convective flows and, consequently, velocity gradients that produce shear forces within the bulk liquid. Therefore, we believe that the shear forces induced by modulation should promote the structural ordered-to-disordered transition in the liquid Vit106a as the overheating temperature increase. This is also the case when using the oscillation drop method but to a lesser extent. The large drop in liquid viscosity due to the ordered-to-disordered transition likely reduces the potential for emergence of dynamic heterogeneities within the undercooled liquid and could explain the improved supercooled liquid state. Numerous molecular dynamics (MD) studies have demonstrated that dynamic heterogeneities in the liquid, particularly regions of low atomic mobility having a high degree of icosahedral symmetry, can act as preferential sites for crystal nucleation [37,38]. Additionally, some studies suggest that shear flow can significantly influence the nucleation process [42].

All those results underscore the beneficial role of high-temperature sinusoidal modulation and rapid quenching in optimizing the liquid thermal processing of the Vit106a alloy. Besides, in the study Gangopadhyay et al., they successfully vitrified a 6 mm Vit106 sphere [17]. However, vitrification was achieved only once, using a combination of high-temperature modulation (1400 K to 1020 K) and He gas quenching ($Q_R \approx 15$ K s^{-1}), while attempts with He quenching alone were unsuccessful. Although the authors attributed this to possible surface oxidation, the critical role of temperature modulation may have been underestimated. In our study, none of the Vit106a thermal cycles performed aboard the ISS combined high-temperature modulation with He-assisted quenching, which may explain the absence of similar vitrification outcomes. However, to confirm whether this effect is genuinely induced by temperature modulation rather than simply resulting from an increased residence time at high temperature, additional experiments are required. In particular, comparative experiments should be performed with and without modulation while maintaining identical residence times in the high-temperature liquid state under controlled isothermal conditions.

5. Conclusion

Our investigation highlights the complex interplay between thermal history, gravity, and processing conditions in determining the vitrification behavior and microstructural evolution of Vit106a alloys. The gravitational segregation of Nb observed in both ground-based and parabolic flight samples, despite the use of a Nb–Ni pre-alloy, suggests that density-driven phase separation during solidification and limited reactivity of Nb with the other elements remains a significant challenge for achieving compositional homogeneity in large samples. In contrast, this segregation was not observed in the ISS-processed sample, where microgravity likely suppressed density-driven separation. We also demonstrate that the Vit106a sample is highly sensitive to heterogenous nucleation, which probability increases as the sample size increases. A key finding of this study is the critical role of thermal processing, in influencing the undercooled liquid behavior of the alloy. Sinusoidal thermal modulation carried out strictly above 1275 K led to a pronounced decrease in T_x by up to 80 K, underscoring its ability to alter nucleation pathways, therefore increasing the supercooled liquid region. In summary, achieving full vitrification in large-scale Vit106a samples depends not only on achieving high cooling rates but also on managing the liquid through controlled thermal processing. These findings emphasize the need for continued investigation into liquid-state dynamics and the development of advanced thermal processing techniques, particularly for applications involving bulk metallic glass components at scale.

Declaration of competing interest

The authors declare that they have no known competing financial interests or personal relationships that could have appeared to influence the work reported in this paper.

Acknowledgement

Funding sources: This work was supported by the ThermoProp-CH project, related to the European Space Agency MAP AO-99-022 and the PRODEX Experiment Arrangement No 4000115323 (PI: AN). The authors would also like to thank Robin Pauer and the Electron Microscopy Center at Empa for the rapid SEM–EDS analysis performed on short notice.

Appendix A. Supplementary data

Supplementary data to this article can be found online at https://doi.org/10.1016/j.jmrt.2026.06.151.

References

[1] Inoue A. Stabilization of metallic supercooled liquid and bulk amorphous alloys. Acta Mater 2000;48:279–306. https://doi.org/10.1016/S1359-6454(99)00300-6.
[2] Yang GN, Shao Y, Yao KF, Chen SQ. A study of cooling process in bulk metallic glasses fabrication. AIP Adv 2015;5(11):117111. https://doi.org/10.1063/1.4935440.
[3] Peker A, Johnson WL. A highly processable metallic glass: Zr41.2Ti13.8Cu12.5Ni10.0Be22.5. Appl Phys Lett 1993;63(17):2342–4. https://doi.org/10.1063/1.110520.

[4] Kim YJ, Busch R, Johnson WL, Rulison AJ, Rhim WK. Metallic glass formation in highly undercooled Zr41.2Ti13.8Cu12.5Ni10.0Be22.5 during containerless electrostatic levitation processing. Appl Phys Lett 1994;65(17):2136–8. https://doi.org/10.1063/1.112768.
[5] Hays CC, Schroers J, Johnson WL, Rathz TJ, Hyers RW, Rogers JR, Robinson MB. Vitrification and determination of the crystallization time scales of the bulk-metallic-glass-forming liquid Zr58.5Nb2.8Cu15.6Ni12.8Al10.3. Appl Phys Lett 2001;79(11):1605–7. https://doi.org/10.1063/1.1398605.
[6] Wei S, Yang F, Bednarcik J, Kaban I, Shuleshova O, Meyer A, Busch R. Liquid–liquid transition in a strong bulk metallic glass-forming liquid. Nat Commun 2013;4(1):2083. https://doi.org/10.1038/ncomms3083.
[7] Stolpe M, Jonas I, Wei S, Evenson Z, Hembree W, Yang F, Meyer A, Busch R. Structural changes during a liquid-liquid transition in the deeply undercooled Z r 58.5 C u 15.6 N i 12.8 A l 10.3 N b 2.8 bulk metallic glass forming melt. Phys Rev B 2016;93(1):014201. https://doi.org/10.1103/PhysRevB.93.014201.
[8] Li JJZ, Rhim WK, Kim CP, Samwer K, Johnson WL. Evidence for a liquid–liquid phase transition in metallic fluids observed by electrostatic levitation. Acta Mater 2011;59(5):2166–71. https://doi.org/10.1016/j.actamat.2010.12.017.
[9] Gallino I, Shah MB, Busch R. Enthalpy relaxation and its relation to the thermodynamics and crystallization of the Zr58.5Cu15.6Ni12.8Al10.3Nb2.8 bulk metallic glass-forming alloy. Acta Mater 2007;55(4):1367–76. https://doi.org/10.1016/j.actamat.2006.09.040.
[10] Gallino I. On the fragility of bulk metallic glass forming liquids. Entropy 2017;19(9):483. https://doi.org/10.3390/e19090483.
[11] Wei S, Stolpe M, Gross O, Evenson Z, Gallino I, Hembree W, Bednarcik J, Kruzic JJ, Busch R. Linking structure to fragility in bulk metallic glass-forming liquids. Appl Phys Lett 2015;106(18):181901. https://doi.org/10.1063/1.4919590.
[12] Evenson Z, Raedersdorf S, Gallino I, Busch R. Equilibrium viscosity of zr–cu–ni–al–nb bulk metallic glasses. Scr Mater 2010;63(6):573–6. https://doi.org/10.1016/j.scriptamat.2010.06.008.
[13] Mukherjee S, Schroers J, Zhou Z, Johnson WL, Rhim W-K. Viscosity and specific volume of bulk metallic glass-forming alloys and their correlation with glass forming ability. Acta Mater 2004;52(12):3689–95. https://doi.org/10.1016/j.actamat.2004.04.023.
[14] Way C, Wadhwa P, Busch R. The influence of shear rate and temperature on the viscosity and fragility of the Zr41.2Ti13.8Cu12.5Ni10.0Be22.5 metallic-glass-forming liquid. Acta Mater 2007;55(9):2977–83. https://doi.org/10.1016/j.actamat.2006.12.032.
[15] Evenson Z, Schmitt T, Nicola M, Gallino I, Busch R. High temperature melt viscosity and fragile to strong transition in Zr–Cu–Ni–Al–Nb(Ti) and Cu47Ti34Zr11Ni8 bulk metallic glasses. Acta Mater 2012;60(12):4712–9. https://doi.org/10.1016/j.actamat.2012.05.019.
[16] Zhang L, Wu Y, Feng S, Li W, Zhang H, Fu H, Li H, Zhu Z, Zhang H. Rejuvenated metallic glass strips produced via twin-roll casting. J Mater Sci Technol 2020;38:73–9. https://doi.org/10.1016/j.jmst.2019.08.022.
[17] Gangopadhyay AK, Sellers ME, Bracker GP, Holland-Moritz D, Van Hoesen DC, Koch S, Galenko PK, Pauls AK, Hyers RW, Kelton KF. Demonstration of the effect of stirring on nucleation from experiments on the international space station using the ISS-EML facility. npj Microgravity 2021;7(1):31. https://doi.org/10.1038/s41526-021-00161-9.
[18] Mukherjee S, Zhou Z, Schroers J, Johnson WL, Rhim WK. Overheating threshold and its effect on Time–temperature-transformation diagrams of zirconium based bulk metallic glasses. Appl Phys Lett 2004;84(24):5010–2. https://doi.org/10.1063/1.1763219.
[19] Fan C, Choo H, Liaw PK. Influences of Ta, Nb, or Mo additions in Zr-Based bulk metallic glasses on microstructure and thermal properties. Scr Mater 2005;53(12):1407–10. https://doi.org/10.1016/j.scriptamat.2005.08.025.
[20] Fan C, Qiao D, Wilson TW, Choo H, Liaw PK. As-Cast zr–ni–cu–al–nb bulk metallic glasses containing nanocrystalline particles with ductility. Mater Sci Eng, A 2006;431(1–2):158–65. https://doi.org/10.1016/j.msea.2006.05.129.
[21] Terebenec D, Mohr M, Wunderlich R, Fecht H-J, Schneider S, Dommann A, Neels A. Thermophysical properties and solidification behavior of liquid Vit106a in microgravity. npj Micrograv 2026;12(1):26. https://doi.org/10.1038/s41526-026-00572-6.
[22] Mohr M, Dong Y, Bracker GP, Hyers RW, Matson DM, Zboray R, Frison R, Dommann A, Neels A, Xiao X, Brillo J, Busch R, Novakovic R, Srirangam P, Fecht H-J. Electromagnetic levitation containerless processing of metallic materials in microgravity: thermophysical properties. npj Microgravity 2023;9(1):34. https://doi.org/10.1038/s41526-023-00281-4.
[23] Arganda-Carreras I, Kaynig V, Rueden C, Eliceiri KW, Schindelin J, Cardona A, Sebastian Seung H. Trainable weka segmentation: a machine learning tool for microscopy pixel classification. Bioinformatics 2017;33(15):2424–6. https://doi.org/10.1093/bioinformatics/btx180.
[24] Schindelin J, Arganda-Carreras I, Frise E, Kaynig V, Longair M, Pietzsch T, Preibisch S, Rueden C, Saalfeld S, Schmid B, Tinevez J-Y, White DJ, Hartenstein V, Eliceiri K, Tomancak P, Cardona A. Fiji: an open-source platform for biological-image analysis. Nat Methods 2012;9(7):676–82. https://doi.org/10.1038/nmeth.2019.
[25] Zeman P, Zítek M, Zuzjaková Š, Čerstvý R. Amorphous Zr-Cu thin-film alloys with metallic glass behavior. J Alloys Compd 2017;696:1298–306. https://doi.org/10.1016/j.jallcom.2016.12.098.
[26] Li M-X, Sun Y-T, Wang C, Hu L-W, Sohn S, Schroers J, Wang W-H, Liu Y-H. Data-driven discovery of a universal indicator for metallic glass forming ability. Nat Mater 2022;21(2):165–72. https://doi.org/10.1038/s41563-021-01129-6.
[27] Okamoto H. Nb-Ni (Niobium–Nickel). J Phs Eqil and Diff 2008;29(2). https://doi.org/10.1007/s11669-008-9277-0. 210–210.
[28] Takeuchi A, Inoue A. Classification of bulk metallic glasses by atomic size difference, heat of mixing and period of constituent elements and its application to characterization of the main alloying element. Mater Trans 2005;46(12):2817–29. https://doi.org/10.2320/matertrans.46.2817.
[29] Jiang H-R, Xu H, Xu L-Z, Gao Y-F, Lu W-F, Mu Y-K, Jia Y-D, Ren J, Zhang B, Wang G. Effect of phase separation induced by Nb microalloying on the glass formation and crystallization of CuZr-Based bulk metallic glasses. J Mater Res Technol 2025;39:873–84. https://doi.org/10.1016/j.jmrt.2025.09.140.
[30] Zhang L, Zhang H. Ti-Based metallic glass composites containing β-Ti dendrites. Prog Mater Sci 2025;152:101472. https://doi.org/10.1016/j.pmatsci.2025.101472.
[31] Zhang L, Yan T, Şopu D, Wu Y, Jiang B, Du K, Zhang H, Eckert J. Shear-band blunting governs superior mechanical properties of shape memory metallic glass composites. Acta Mater 2022;241:118422. https://doi.org/10.1016/j.actamat.2022.118422.
[32] Sosso GC, Chen J, Cox SJ, Fitzner M, Pedevilla P, Zen A, Michaelides A. Crystal nucleation in liquids: open questions and future challenges in molecular dynamics simulations. Chem Rev 2016;116(12):7078–116. https://doi.org/10.1021/acs.chemrev.5b00744.
[33] Díaz Leines G, Michaelides A, Rogal J. Interplay of structural and dynamical heterogeneity in the nucleation mechanism in nickel. Faraday Discuss 2022;235:406–15. https://doi.org/10.1039/D1FD00099C.
[34] Busch R, Schneider S, Peker A, Johnson WL. Decomposition and primary crystallization in undercooled Zr41.2Ti13.8Cu12.5Ni10.0Be22.5 melts. Appl Phys Lett 1995;67(11):1544–6. https://doi.org/10.1063/1.114487.
[35] Löffler JF, Johnson WL. Model for decomposition and crystallization of Zr-Based bulk amorphous alloys near the glass transition. Mater Sci Eng, A 2001;304–306:670–3. https://doi.org/10.1016/S0921-5093(00)01561-6.
[36] Gómez LR, Vega DA. Amorphous precursors of crystallization during spinodal decomposition. Phys Rev E 2011;83(2):021501. https://doi.org/10.1103/PhysRevE.83.021501.
[37] Puosi F, Jakse N, Pasturel A. Dynamical, structural and chemical heterogeneities in a binary metallic glass-forming liquid. J Phys Condens Matter 2018;30(14):145701. https://doi.org/10.1088/1361-648X/aab110.
[38] Zanotto ED, Montazerian M. Dominant effect of heterogeneous dynamics on homogenous crystal nucleation in supercooled liquids. Front Phys 2020;8:20. https://doi.org/10.3389/fphy.2020.00020.
[39] Mohr M, Wunderlich RK, Hofmann DC, Fecht H-J. Thermophysical properties of liquid Zr52.5Cu17.9Ni14.6Al10Ti5—Prospects for bulk metallic glass manufacturing in space. npj Microgravity 2019;5(1):24. https://doi.org/10.1038/s41526-019-0084-1.
[40] Lin XH, Johnson WL, Rhim WK. Effect of oxygen impurity on crystallization of an undercooled bulk glass forming zr–ti–cu–ni–al alloy. Mater Trans JIM 1997;38(5):473–7.
[41] Bendert JC, Blodgett ME, Gangopadhyay AK, Kelton KF. Measurements of volume, thermal expansion, and specific heat in Zr57Cu15.4Ni12.6Al10Nb5 and Zr58.5Cu15.6Ni12.8Al10.3Nb2.8 liquids and glasses. Appl Phys Lett 2013;102(21):211913. https://doi.org/10.1063/1.4808030.
[42] Mura F, Zaccone A. Effects of shear flow on phase nucleation and crystallization. Phys Rev E 2016;93(4):042803. https://doi.org/10.1103/PhysRevE.93.042803.